AIAA AVIATION Forum
June 15-19, 2020, VIRTUAL EVENT
AIAA AVIATION 2020 FORUM

10.2514/6.2020-3014

Experimental Drag Study of the Bio-inspired Body Shape

Svetlana V. Poroseva[1], Derrick Charley[2], Peter Vorobieff [3]
University of New Mexico, Albuquerque, NM, 87131, U.S.A.

Aerodynamics of short axisymmetric bodies is of importance for the rotorcraft design and operation, where many parts have such shapes or can be represented as a group of such bodies. Of interest for the current study is the drag contribution from a combined shape of the assembly of a proprotor (excluding blades) and a nacelle, the proprotor is attached to. Such an assembly is a common feature in existing tiltrotors and also in many proposed designs of future air taxis. However, experimental and numerical data are scarce in this research area. Our paper presents results of an experimental study, in which we sought to understand whether a bio-inspired shape of the proprotor-nacelle assembly could be beneficial for the drag reduction. Following our previous works on bio-inspired rotor blade designs, the tested bio-inspired proprotor-nacelle assembly design was based on the Cicada body shape. For comparison, experiments were also conducted with other three bodies of the same cross section: short circular cylinder, double bullet, and an ellipsoid based on the V-22 Osprey assembly adopted from NASA publications. In the experiments, all designs were axially oriented with the flow direction at a zero-degree angle of attack, corresponding to the forward horizontal flight. The Reynolds number range was up to 40,000, with incoming flow being laminarized. The drag measurements and flow visualizations were conducted in the water tunnel at the Department of Mechanical Engineering, University of New Mexico.

I. Nomenclature

A	=	cross-sectional area
C_d	=	drag coefficient
d	=	diameter
D	=	Drag
l	=	length
Re	=	Reynolds number based on diameter of the design maximum cross-section.
U_∞	=	freestream velocity
ν	=	kinematic viscosity
ρ	=	density

II. Introduction

With city populations and car traffic growing, the futuristic idea of moving from ground to air transportation for commuting has attracted a lot of interest from car and aircraft industries [1-3]. NASA has been working on advancing related vehicle concepts since 2011 and launched the Urban Air Mobility (UAM) program in 2017 hoping to bring

[1]Associate Professor, Department of Mechanical Engineering, University of New Mexico, Albuquerque, NM 87131, AIAA Associate Fellow
[2]Undergraduate student, Department of Mechanical Engineering, University of New Mexico, Albuquerque, NM 87131, AIAA Student Member
[3]Professor, Department of Mechanical Engineering, University of New Mexico, Albuquerque, NM 87131, AIAA Associate Fellow

the dream of air commuting to reality by 2020 in collaboration with Uber [4,5]. FAA is also involved in developing regulations to facilitate safe low-altitude flying [6]. The American Institute of Aeronautics and Astronautics hosted the panel "Dude, Where's My Flying Car" at the 2018 AIAA SciTech Forum [7]. Google search produced 68,800,000 references for "flying car concept" (popular, but wrong expression) in less than a second (in May, 2020).

The majority of low-altitude flying aircraft concepts rely on using rotors, with many of those concepts being tiltrotorcrafts to provide a vehicle with the ability of vertical takeoff/landing and hovering as traditional helicopters do, but also allowing forward flight with efficiency superior to helicopters in urban landscapes.

In tiltrotocrafts, a rotor similar to one used in traditional helicopters provides vertical thrust during takeoff, landing, and hovering, and can be tilted in a forward-facing position to act as a propeller in forward horizontal flight. For this reason, rotors in tiltrotorcrafts are often called "proprotors".

It remains unknown in an optimal approach exists to design, mounting, and operation of proprotors in air taxis. Existing tiltrotors such as, for example, V-22 Osprey have proprotors mounted on the top of nacelles that tilt to switch form one flight stage to another. Such an assembly is the focus of the current study.

The nacelles host engines and other equipment relevant to the proprotors operation [8]. Their dimensions are significant, and one should expect significant contribution from proprotors and nacelles to drag experienced by the tiltrotorcraft during every flight stage. Literature on this subject is not readily available for tiltrotors, but in helicopters the rotor hub alone can contribute for up to 30% of the vehicle drag [9-10]. Moreover, new studies focused specifically on air taxis are required, as they will be smaller and lighter than existing tiltrotorcrafts, and so will be their proprotors and nacelles. Scaling, however, is known to be problematic when rotors are involved [11-14].

The current study investigates the shape effect of a simplified proprotor-nacelle assembly represented by an axisymmetric body (red dashed line in Fig. 1) on drag when the body is axially aligned with the flow at a zero-degree angle of attack (facing forward towards the incoming flow). Visualization of the flow around the body is also provided. All other effects are excluded from the current research.

Shapes considered are:

- a generic finite circular cylinder with a small length-to-diameter ratio (Fig. 2a),
- a double bullet, which is a short circular cylinder with smoothed hemispherical ends (Fig. 2b),
- an ellipsoid based on the V-22 Osprey assembly reconstructed from Ref. [15] describing rotor simulations in hover mode (Fig. 2c),
- a bio-inspired design (Fig. 2d).

All designs are three-dimensional (3D) with a circular cross-section at any location along the bodies' length. The largest cross-sectional areas in all designs are equal.

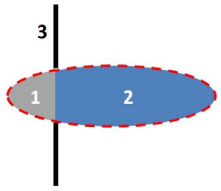

Fig. 1. A simplified representation of the proprotor-nacelle assembly considered in the current study. Notation: 1 – proprotor, 2 – nacelle, 3 – rotor plane.

In continuation of our previous studies [16-18], an insect, whose body is used as the design prototype belongs to the Cicada sp. In Ref. [16], we concluded from the qualitative analysis and a very basic quantification of insect characteristics that cicadas are the best-suited candidates to look for aerodynamic features which can be potentially useful for application in small rotorcrafts.

There are very limited data available on aerodynamics of finite 3D bodies with a small length-to-diameter ratio, and in particular, when a body is in the face-forward position with respect to the flow direction. Here, experimental and numerical data from Ref. [19] and [20], respectively, are used. In [19], data are available for cylinders and disks. Ref. [20] describes simulations for a finite circular cylinder with the length-to-diameter ratio between one and two at three Reynolds numbers (based on the cylinder diameter): $0.96 \cdot 10^5, 1.56 \cdot 10^5$, and $1 \cdot 10^6$, and at various yaw angles.

The experiments demonstrated the drag reduction when the length-to-diameter of a circular cylinder increased from zero to two. After that, drag stabilizes. Simulations found no sensitivity of drag to the Reynolds number within the considered parameters ranges, when a cylinder is axially aligned with the flow. It was also found that when the ratio $l/d = 1$, the cylinder drag is equal to that of the circular disk. At $l/d = 2$, results agreed with experimental data for the finite cylinder from Ref. [19].

In the current study, experiments in the water tunnel at the Department of Mechanical Engineering, University of New Mexico were conducted. Drag measurements were acquired at Reynolds numbers up to 40,000 and flow visualizations were acquired at Reynolds numbers less than 1000. All designs were scaled to fit the experimental facilities, facilitating appropriate blockage ratio (not to exceed 5%). At the current research stage, we did not attempt

to match the flow conditions of a realistic forward flight, but to explore advantages (if any) of the bio-inspired design within the range constrained by available facilities.

III. Designs

The starting point of designing the bio-inspired body was approximation of a real Cicada body (based on collected deceased specimens) as an axisymmetric body. The real Cicada body is not axisymmetric and has 3D features omitted from our design.

The photograph of the Cicada (Fig. 3a) was used in Inkscape [21] to determine relevant dimensions shown in mm in Fig. 3c. Figure 3b shows the Cicada image with the superimposed design planform. No statistical analysis was conducted to find average dimensions for the Cicada body as they are not easy to find unless in certain years. Instead, visual comparison with a few other cicadas found in the same geographical location was made to ensure that the one we used as a prototype has a commonly shaped body. Generally, the length of real cicadas lies in the range between 22 and 55 mm.

In a similar fashion, that is, using an image from the NASA simulation of a flow produced by the V-22 Osprey rotor [15], dimensions of the ellipsoid representing the proprotor-nacelle assembly in the V-22 Osprey were determined (Fig. 3d).

Notice that both bio-inspired and ellipsoid designs have the same distance between the nose and the location of the wings and blades: 10.50 mm. They also have the same radius at this location: 8.75 mm. Keeping all proportions unchanged led to the bio-inspired design being longer: 30.7 mm vs. 22.16 mm of the ellipsoid length from the wings/blades location.

The designs whose dimensions are shown in Figs. 3c and 3d were used in preliminary simulations [18], but not in the current paper. For the current study, they were enlarged, with their dimensions shown in Table 1.

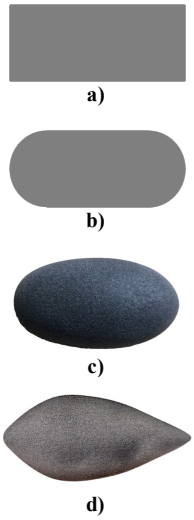

Fig. 2. Considered shapes of the proprotor-nacelle assembly (not to scale): a) cylinder, b) double bullet, c) ellipsoid, d) bio-inspired design.

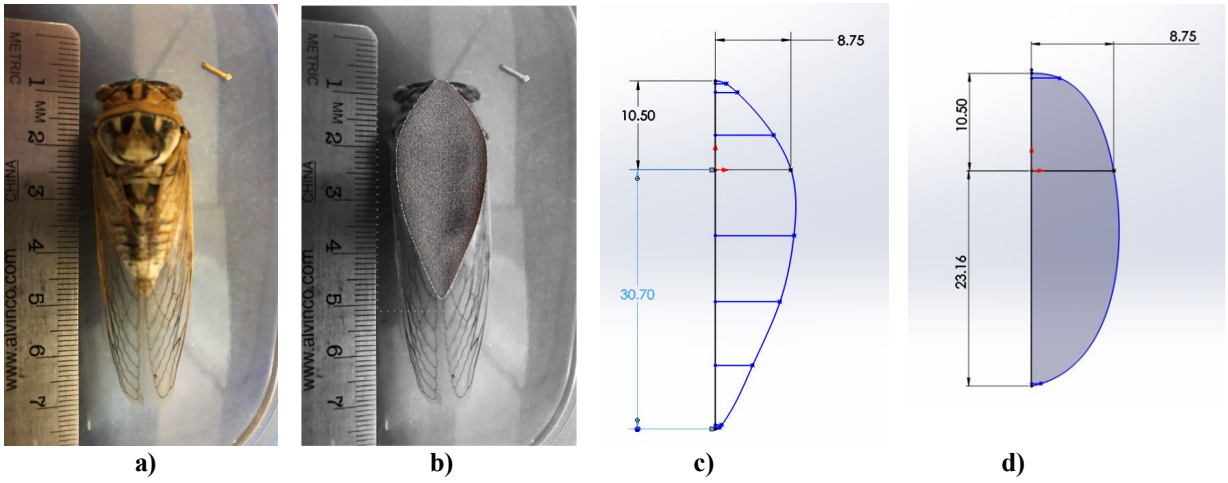

Fig. 3. Photo of a real Cicada used in the study made by Erich Brown for [18] (a), the same photo with the imposed image of the design planform (b), dimensions for a half of the bio-inspired body design in (mm) from Ref. [18] (c), dimensions for a half of the ellipsoid design in mm from Ref. [18] based on the V-22 Osprey model from Ref. [15].

TABLE 1. Dimensions of the designs.

	Cylinder	Double Bullet	Bio-inspired	Ellipsoid
Max cross-sectional Area (mm^2)	1093.88	1093.88	1093.88	1093.88
Length (mm)	68.82	68.82	82.33	68.82

Note that the maximum cross-sectional areas of the bio-inspired body and of the ellipsoid are equal and correspond to the body diameter of d = 37.32 mm. The distance between the nose and the maximum cross-sectional area is not the same in two designs.

The lengths of two designs are different to preserve shapes of the original designs [18]. Thus, the length-to-diameter ratio of the bio-inspired design is 2.21 and that of the ellipsoid is 1.84.

The designs were generated using the CAD package Solidworks.

To compare with the existing experimental and numerical data [19,20], CAD models were also created for the 3D cylinder and for the double bullet, both having the same length and diameter as the ellipsoid. The double bullet design has smoothed hemispherical ends with the same diameter as that of the body maximum cross-section (Fig. 4).

The CAD models were 3D printed at high resolution from nylon by WESTWIND company located at Albuquerque, NM.

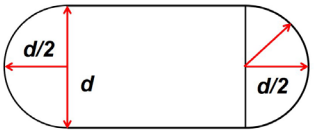

Fig. 4. Schematic representation of the double bullet design.

IV. Experimental Setup

Experiments were carried out using the ELD 501 closed-loop water tunnel in the Fluids Lab at the Department of Mechanical Engineering, University of New Mexico (Fig. 5). The water tunnel has a 6 in x 6 in. cross-sectional test area. The tunnel is equipped with intake flow-conditioning honeycombs that enable the flow to remain laminar even at higher speeds. The flow speed is controlled by a variable frequency drive (VFD in the range between 0 – 0.98 m/s. The measurements were acquired at 20°C water temperature. The water density was $\rho = 998.2$ kg/m^3, and the kinematic viscosity $\nu = 1.004 \cdot 10^{-6}$ m^2/s.

For flow visualization, dye (food coloring) diluted with water was introduced into the flow stream to visualize the streaklines.

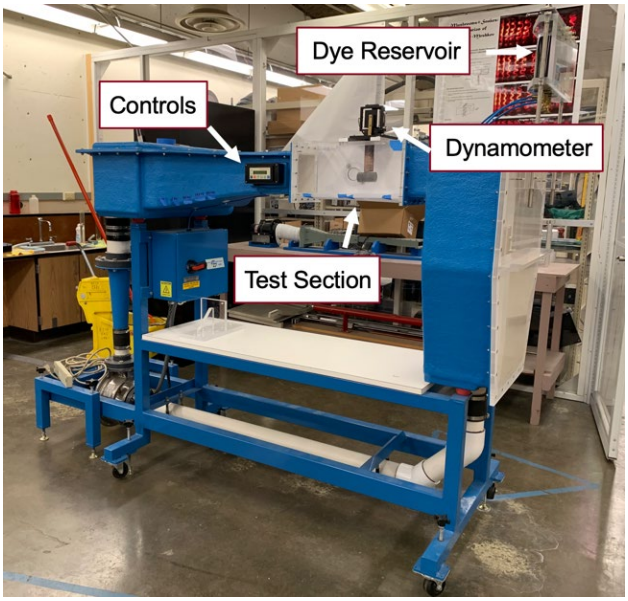

Fig. 5. The water tunnel used in the experiments.

V. Drag Measurements

Each shape shown in Fig. 2 with dimensions summarized in Table 1 was mounted on the arm of a two-axis (lift/drag) ELD balance using LVDT (linear variable displacement transducers) to produce force measurements. Figure 6 presents results obtained for the drag force in *N* and for the drag coefficient. The drag coefficient is defined as

$$C_d = \frac{D}{\left(\frac{\rho U_\infty^{\ 2}}{2}\right) A}.$$

The measurement uncertainty analysis was carried out following standard procedure described in Ref. [22]. For the drag force uncertainty, the mean drag force D and its standard deviation S_d were computed based on at least thirty experimental readings. Then the total uncertainty was assessed as

$$w_D = \sqrt{w_c^2 + (t\, S_d)^2}\ ,$$

where $t = 2$ corresponds to the 95% confidence level and the sample size over thirty. These uncertainty intervals are represented by the error bars in Fig. 6a. For the drag coefficient, we had accounted both for the uncertainty in D (dominated by data repeatability) and the uncertainty w_U of the freestream velocity U_∞, which, from manufacturer data, did not exceed 0.02 m/s:

$$w = \sqrt{\left(\frac{\partial C_D}{\partial D}\, w_D\right)^2 + \left(\frac{\partial C_D}{\partial U} w_U\right)^2}$$

At lower values of the Reynolds number, uncertainty in the freestream velocity was the dominant contribution to the error bars (again corresponding to the 95% confidence intervals) in Fig. 6b.

The results for the cylinder can be compared with those in Refs. [19, 20]. In the three studies, the cross-sectional area was used in the drag coefficient definition. Moreover, the length-to-diameter ratio used in our work (1.84) falls between the ratios used in [20]: 1 and 2. The maximum Reynolds number considered in the current study, $3.64 \cdot 10^4$, is close to the smallest Re in Ref. [20]: $9.6 \cdot 10^4$.

In Ref. [20], the effect of the Reynolds number variation was not significant within the considered range of values. However, the effect of the *l/d* ratio was found to be strong, causing the drag coefficient to vary between 0.85 and 1.17 (Fig. 4b in Ref. [20]), with the largest value of 1.17 corresponding to the smallest *l/d* ratio of one. Strong dependence on the *l/d* ratio when this ratio is less than 2 was also reported in Ref. [19].

Our drag measurements show the drag coefficient dependence on the Reynolds number as its value reduces and particularly, for lower *Re*, but the measurement uncertainty is also high at these values. At the maximum Reynolds number in our study, $3.64 \cdot 10^4$, the drag coefficient for the cylinder, 0.93±0.02, which is close to the values obtained in Refs. [19,20] at $l/d \leq 2$ (Fig. 4b in [20]) : 0.86 and 0.85, respectively. Notice that surface roughness is likely to affect the drag values in the experiments, but it was disregarded in the simulations [20]. The 3D printing procedure used for our models did introduce a noticeable surface roughness, but it was consistent for all the models. Overall, we conclude based on the results of our measurements for the cylinder that the quality of our data is sufficient to proceed with the comparison of the performance of different designs for the proprotor-nacelle assembly.

There is a difference between the design performance at $Re < 15{,}000$ and $Re > 15{,}000$, so the data will be compared separately for these two regions.

At the lowest Reynolds number assessed, *Re* = 1375, the measured values of the drag force for all the shapes are in the *mN* range, and the resulting uncertainty makes it difficult to interpret the results for the drag coefficient. However, the ellipsoid based on the V-22 Osprey assembly from NASA simulations [15] has the drag coefficient close to that of the cylinder. At this lowest *Re*, the average drag coefficient value for the cylinder is 0.92, while the value for the flat disk from [19] of 1.17. For the next three Re values, 5950, 9670, and 12270, the double bullet has the highest drag coefficient.

On the other hand, the bio-inspired design consistently has drag either lower than or statistically indistinguishable from (at lowest *Re*) the other three designs in this range.

With the Reynolds number increasing, the drag coefficient for the bio-inspired design decreases to about 0.023 at $Re = 3.64 \cdot 10^4$. Similar drag coefficients were reported (of course, for much higher Reynolds numbers) for several

airships from the golden age of flight [23]. The double bullet outperforms the cylinder and the ellipsoid at $Re > 15{,}000$, but the difference between the drag coefficients of the double bullet and the ellipsoid is modest, about 6±1%.

VI. Flow Visualization

Flow visualization was performed at three different velocities corresponding to three different Reynolds numbers: 280, 420, and 560. Three different dye-injection streaklines were observed to develop a better understanding of the flow patterns experienced by the shapes of each rotor hub. The following figures are screenshots taken from the videos.

At all considered Reynolds numbers, the wake with recirculation developed behind the cylinder is far more prominent than for any other shape (Figs. 7-10), which should be expected for a blunt body. Another recirculation

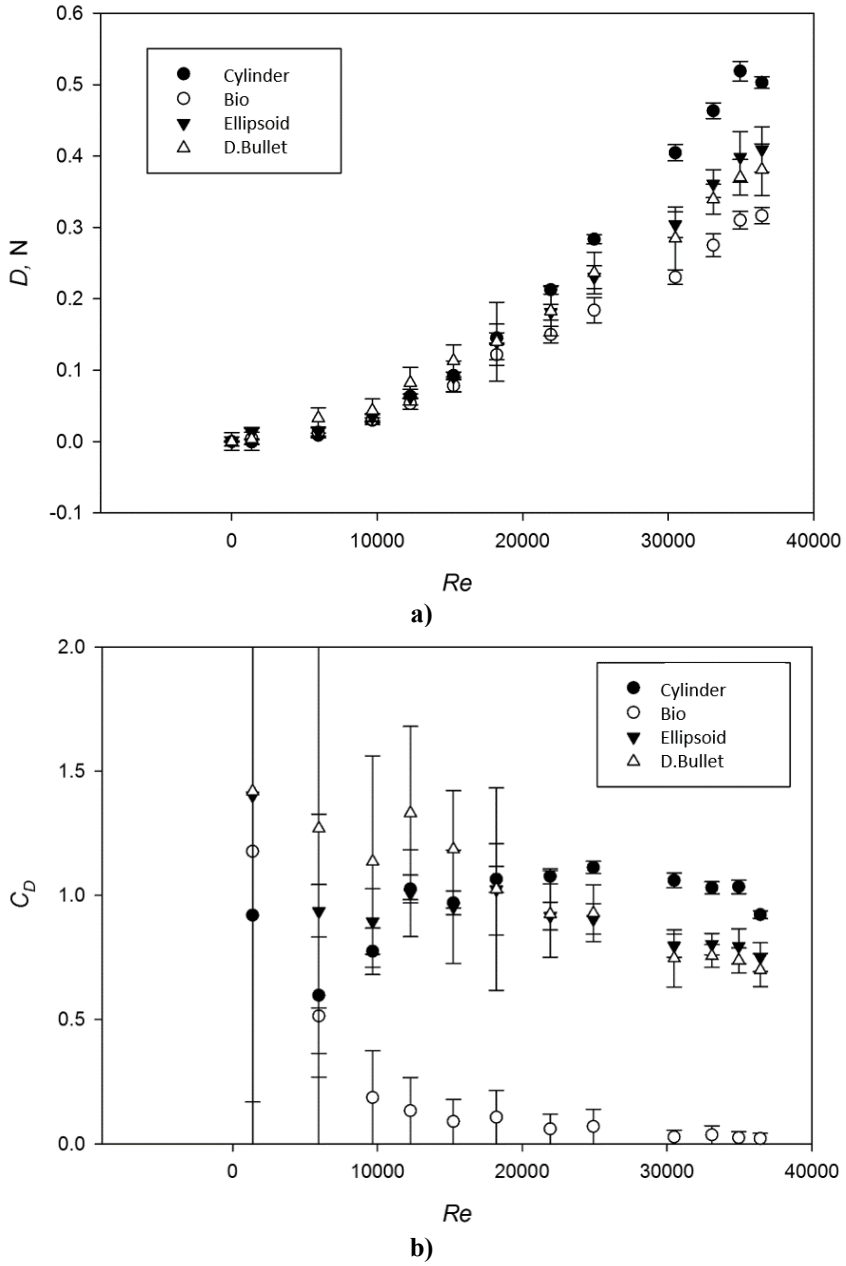

Fig. 6. Drag (a) and the drag coefficient (b) for four designs considered in the study as functions of the Reynolds number.

zone can be seen forming below the cylinder (Fig. 10). In addition, a disturbance ahead of the cylinder is clearly observed when looking at the flow around the cylinder from above (Fig. 10).

The wake flow behind the double bullet remains smooth at the three Reynolds numbers, with no observed separation zone to occur at any location. Some small disturbances can be noticed in the wake of this design at Re = 420 (Fig. 8), but they disappear at higher Re.

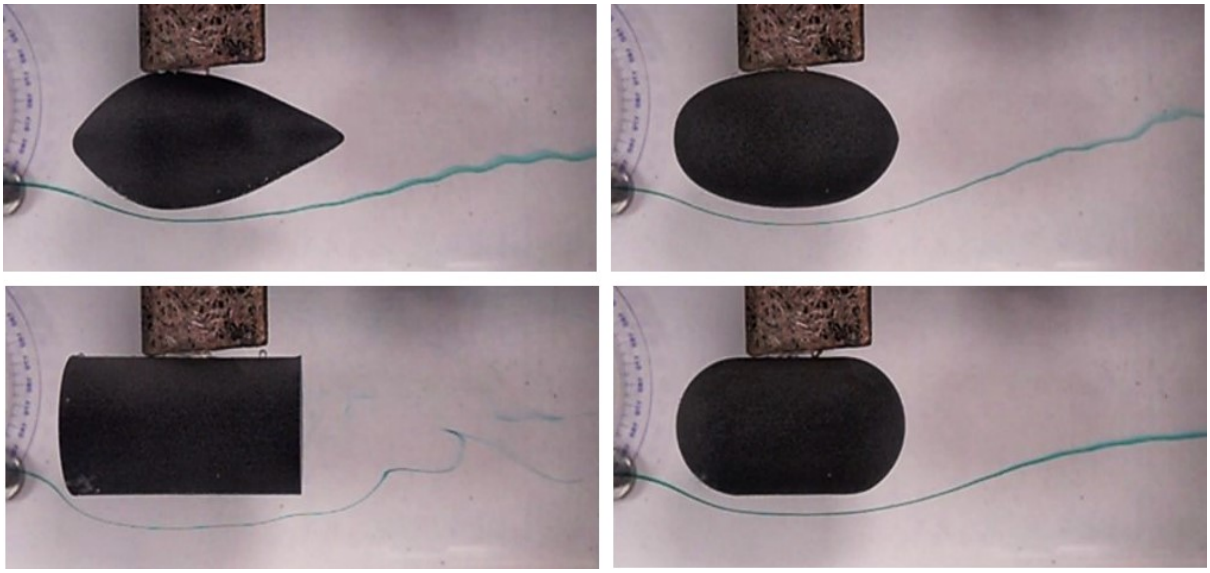

Fig. 7. Flow visualization from the water tunnel experiment taken at Re = 280.

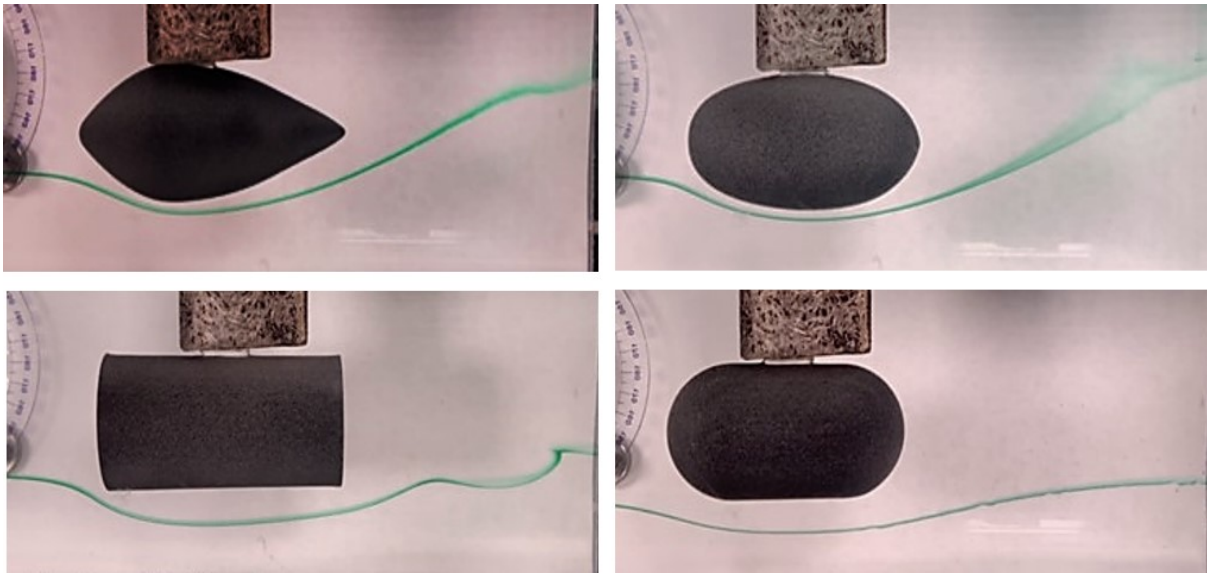

Fig. 8. Flow visualization from the water tunnel experiment taken at Re = 420.

Disturbances are observed behind the ellipsoid at lower Reynolds numbers, but no separation zone could be seen at any Re. At the highest Reynolds number of 560, the wakes behind the double bullet and the ellipsoid look similar. At any of considered Reynolds numbers, the streakline follows the ellipsoid shape closer than that of the double bullet.

Disturbances in the wake behind the bio-inspired design are clearly observed at the lowest Reynolds number (Fig. 7). They gradually disappear with the Reynolds number increasing, but the streakline remains more diffused at the highest Re than those behind the ellipsoid and the double bullet (Fig. 9). No separation zone was observed around this

design in the considered range of the Reynolds number. Overall, the increase of the Reynolds number has stabilizing effect on the flow development around the three designs: bio-inspired one, double bullet, and ellipsoid.

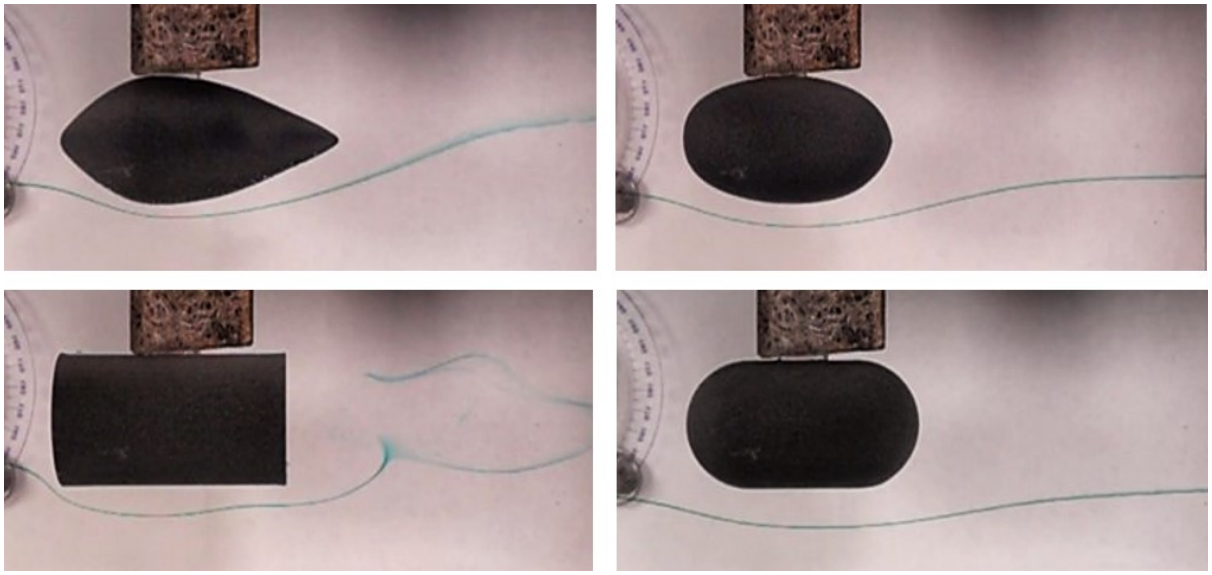

Fig. 9. Flow visualization from the water tunnel experiment taken at *Re* = 560.

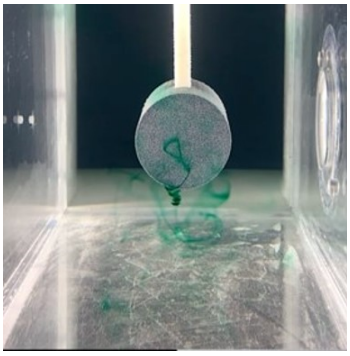

a)

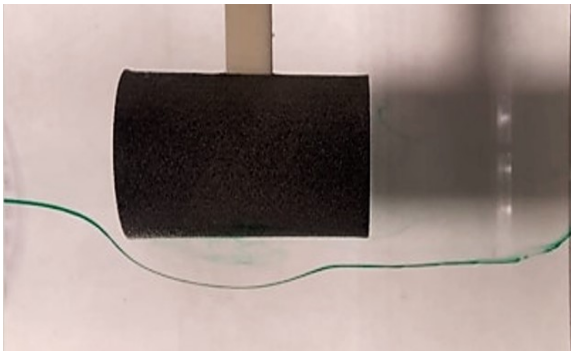

b)

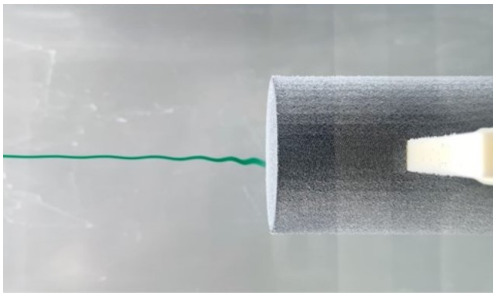

c)

Fig. 10. Flow visualization of the flow around the cylinder at *Re* = 560: a) side view, b) view from behind, c) top view of the flow in front of the cylinder.

VII. Conclusions

We have conducted flow visualization and drag measurements for three possible proprotor-nacelle assembly (ellipsoid, double bullet, and a biologically inspired shape) and for a reference shape (cylinder), in a range of Reynolds numbers up to about 36,400. At the upper limit, the drag coefficient of the reference shape is close to values earlier reported in Refs. [19] and [20] at $l/d \leq 2$ (Fig. 4b in [20]). Our drag measurements also show that over most of the range of velocities we studied, the biologically inspired design outperforms all others: cylinder, ellipsoid, and double-bullet. This provides us with motivation to continue studies of biologically-inspired designs, beginning with an investigation of the effects of non-zero angles of attack on the lift and drag of the models described here. Extending the range of Reynolds numbers for future work is also highly desirable.

Acknowledgments

Derrick Charley would like to thank the McNair Scholars Program for supporting his research during this project. Dr. Svetlana V. Poroseva would like to acknowledge a partial support from the UNM RAC for this study. The authors express their gratitude to WESTWIND (Albuquerque, NM) for 3D printing the designs. Initial CAD models for all designs were created by Erich Brown, when a graduate student at the UNM ME Department, and by Joshua Dell, when on internship at the UNM ME Department from the Hope Christian High School. Dassault Systèmes provided SolidWorks for academic purposes. We would also like to thank Dr. Patrick Wayne and graduate students Ranjith D. Janardhana, Daniel Freelong and P. Christopher Scott for their help at different stages of the experiments, as well as the senior machinist Jason Church for advising on the designs manufacturing process, all at the UNM ME Department.

References

[1] Johnsson, J., and Levin, A., "Boeing Hops on the Flying Car Ban*dw*agon," *Bloomberg*, March 03, 2018. URL: https://skift.com/2018/03/03/boeing-hops-on-the-flying-car-bandwagon/ [retrieved 14 May 2020].

[2] Hawkins, A. J., "Bell Helicopter offers a sneak peek of its first electric flying taxi," *The Verge*, January 8. 2018. URL: https://www.theverge.com/2018/1/8/16865404/bell-helicopter-electric-air-taxi-uber-ces-2018 [retrieved 14 May 2020].

[3] Hawkins, A. J., "Uber's 'flying cars' could arrive in LA by 2020 — and here's what it'll be like to ride one," *The Verge*, November 7. 2018. URL: https://www.theverge.com/2017/11/8/16613228/uber-flying-car-la-nasa-space-act [retrieved 14 May 2020].

[4] Risen, T., "Uber, NASA: Stop saying "flying cars," *Aerospace America*, July/August 2017. URL: https://aerospaceamerica.aiaa.org/departments/uber-nasa-stop-saying-flying-cars/ [retrieved 14 May 2020].

[5] NASA, "NASA Embraces Urban Air Mobility, Calls for Market Study," (Ed. L. Gipson) 7 November, 2017. URL: https://www.nasa.gov/aero/nasa-embraces-urban-air-mobility [retrieved 14 May 2020].

[6] Nelson, S., "FAA braces for flying cars that now require no license or registration," *Washington Examiner*, August 14, 2018. URL: https://www.washingtonexaminer.com/news/faa-braces-for-flying-cars-that-now-require-no-license-or-registration [retrieved 14 May 2020].

[7] Risen, T., "Mainstreaming Urban Air Mobility," *Aerospace America*, 10 January, 2018. *Aerospace America*, URL: https://www.aiaa.org/news/news/2018/01/11/mainstreaming-urban-air-mobility [retrieved 14 May 2020].

[8] The Aviation Zone, "Bell/Boeing V-22 Osprey." URL: https://www.theaviationzone.com/factsheets/v22_features.asp [retrieved 14 May 2020].

[9] Reich, D., Shenoy, R., Smith, M., and Schmitz, S., "A Review of 60 Years of Rotor Hub Drag and Wake Physics: 1954-2014," *J. American Helicopter Society*, Vol. 61, No. 2, 2016, pp. 1- 17. https://doi.org/10.4050/JAHS.61.022007.

[10] Khier, W., "Numerical Analysis Of Hub And Fuselage Interference To Reduce Helicopter Drag," *Proc. 38th European Rotorcraft Forum*, Amsterdam, Netherlands, September 4-7, 2012. Available at *Electronic Library: Publications of DLR*, pp.1-19. URL: https://elib.dlr.de/83001/1/erf_paper_146_2012.pdf [retrieved 14 May 2020].

[11] Williams, R., and Montana, P., "A Comprehensive Plan for Helicopter Drag Reduction," *Proc. American Helicopter Society Symposium on Helicopter Aerodynamic Efficiency*, Hartford, Connecticut, March 1975.

[12] Keys, C. N., and Rosenstein, H., "Summary of Rotor Hub Drag Data,"NASATR NASA CR-152080, 1978.

[13] Churchill, G., and Harrington, R., "Parasite-Drag Measurements of Five Helicopter Rotor Hubs," NASA TM 1-21-59L, 1959.

[14] Reich, D., Willits, S., and Schmitz, S., "Scaling and Configuration Effects on Helicopter Rotor Hub Interactional Aerodynamics," *J. Aircraft,* Vol. 54, No. 5, September–October 2017, pp. 1692-1704. DOI: 10.2514/1.C034250.

[15] Chaderjian, N. M., "High Fidelity Navier-Stokes Simulation of Rotor Wakes." URL: https://www.nas.nasa.gov/SC11/demos/demo1.html [retrieved 14 May 2020].

[16] Gomez, S., Gilkey, L. N., Kaiser, B. E., and Poroseva, S. V., "Computational analysis of a tip vortex structure shed from a bio-inspired blade," AIAA 2014-3253, Proc. The 32nd AIAA Applied Aerodynamics Conference, AIAA AVIATION Forum, Atlanta, GA, 16-20 June, 2014. https://doi.org/10.2514/6.2014-3253

[17] Hintz, C., Khanbolouki, P., Perez, A. M., Tehrani, M., and Poroseva, S. V., "Experimental study of the effects of biomimetic blades and 3D printing on the performance of a small propeller," AIAA 2018-3645, Proc. The 2018 Applied Aerodynamics Conf., AIAA AVIATION Forum, Atlanta, GA, 25-29 June, 2018. https://doi.org/10.2514/6.2018-3645

[18] Brown, E., "Computational Analysis of Rotor Hub Effects," M.S. Project Report, Mechanical Engineering Dept., University of New Mexico, Albuquerque, NM, 2019.
[19] Hoerner, S., *Fluid-Dynamic Drag*, Hoerner Fluid Dynamics, Midland Park, NJ, 1958.
[20] Prosser, D. T., and Smith, M. J., "Aerodynamics of Finite Cylinders in Quasi-Steady Flow," AIAA 2015-1931, Proc. The 53rd AIAA Aerospace Sciences Meeting, Kissimmee, FL, 5-9 January, 2015. https://doi.org/10.2514/6.2015-1931.
[21] Inkscape Draw Freely, Software package, Version 0.92, URL: https://inkscape.org/ [retrieved 14 May 2020].
[22] Wheeler, A. J., and Ganji, A. R., *Introduction to Engineering Experimentation*, 3rd ed., Pearson, Upper Saddle River, NJ, USA, 2010.
[23] Thompson, F.L., and Kirschbaum, H.W., "The drag characteristics of several airships determined by deceleration tests. NACA-TR-397," 1932.